Chapter 5

Dual-Core photonic crystal fiber based plasmonic sensor for a broad range of refractive index sensing

In this chapter, a dual – core PCF sensor based on the surface plasmon resonance phenomenon has been designed and simulated. This PCF sensor is compatible with an extended range of analyte sample detection refractive index range $n_a = 1.21 - 1.39$. *There is a coating of plasmonic material gold (Au) with an adhesive layer of* TiO_2 *which works as a catalyst to enhance the sensing performance coated at the outer region of PCF. The wavelength and amplitude interrogation methods have been applied to detect the sensor's sensitivity. Fabrication through the stack and draw method has been described briefly. Due to the wide range of analyte detection, the proposed sensor structure has many applications, like different types of alcohol detection, pregnancy testing, and different acids and chemical detection.*

Chapter 5: Dual – core PCF based refractive index sensor

5.1 Introduction

Surface plasmon resonance (SPR) is an emerging technology in the different sensing fields, which is a label-free and real-time technique [120]. Sensor with SPR technology has widespread applications in the area, such as bio imaging [170], environmental monitoring [171], food monitoring [172], etc. This phenomenon is a collective oscillation of free electrons (e^-) at the metal and dielectric interface due to interlinkage with evanescent waves. In the earlier stage of SPR technology, a prism-based SPR sensing method was developed. The first method was named the Otto configuration, in which there is a prism and then an air gap followed by a metal layer arrangement. The light strike on the prism base at an angle (θ) larger than the attenuated total reflection angle (θ_{ATR}) for excitation of surface plasmon wave (SPW). Improving this Otto configuration, Kretschmann used a conducting (metal) layer in contact with a prism in his setup and kept it in direct contact with the unknown analyte sample. Now, when (p - polarized) light fall at the prism metal interface at an angle ($\theta \geq \theta_{ATR}$), an evanescent wave is generated, which excites quanta known as surface plasmon moving parallel to the surface. When the power and frequency of the evanescent wave match the power and frequency of the surface plasmon wave (SPW), resonance occurs. This peculiar frequency is known as resonance frequency, and the phenomenon is called surface plasmon resonance[88]. Although this prism-based SPR setup improved sensitivity, it was a costly device with a bulky size with limited mechanism [122]. So we need to find an alternative to this arrangement, and conventional optical fibers were looked upon for this purpose. Conventional optical fibers have mechanical stability for sensing with low confinement losses. Still, there was an issue with removing the outer jacket of fiber chemically or physically to bring the core directly into contact with the sensing region, which makes it fragile. Also, optical fiber lacks tuning parameters, limiting its application in different fields [123].

Chapter 5: Dual – core PCF based refractive index sensor

Photonic crystal fibers (PCFs) have become an emerging option for conventional optical fiber due to their flexible shape, different tunable geometrical parameters, and minimum size. PCFs are a single material fiber (usually fused silica) that have a solid core with finite air holes available in cladding zone that makes a suitable condition of total internal reflection (TIR), and this kind of fiber is known as solid core photonic crystal fiber [124]. Results obtained from PCF structures are far better than conventional optical fiber regarding confinement loss and sensitivity [90]. Two kinds of sensing mechanisms are available to utilize PCF sensors. The first sensing mechanism is an internal coating-based sensing mechanism in which a plasmonic Nano layer is polished around an air hole of the cladding, and an analyte is filled inside this air hole [73 91]. Some research papers have been reported using internal coating-based sensing mechanisms [74 125]. Rifat et al. have announced an internal coating approach based sensor having maximum wavelength sensitivity (WS) obtained 3000 nm/RIU for sample of refractive index (RI) range 1.46 - 1.49, and a maximum resolution R = 2.4×10^{-5} RIU [73]. In this mechanism, cleaning the air hole every time to fill different analytes again is a challenging task in actual practice. Coating the air holes with plasmonic material with uniformity is also tricky. So due to these imperfections seen in the first mechanism, we move forward to the second mechanism, which is known as the external coating sensing mechanism. The plasmonic layer is coated on the outermost portion of the PCF structure so that it can be directly touch with the analyte, which is needed to be sensed [75 127 76]. Paul et al. have worked on the external coating-based mechanism and earned maximum wavelength sensitivity (WS) 11,700 nm/RIU for sample RI range of 1.33 – 1.41 [77].

Based on the fabrication process, detection, and operating method, this mechanism is easier and more comfortable than the previous one, so we have used this external coating sensing mechanism for our research [152].

Our study has presented a photonic crystal fiber with dual-Core (DC-PCF). Our PCF sensor has focused on an extended range of analytes sample range RI 1.21 to 1.39, from lower analyte (RI) to higher analyte (RI). As mentioned above, we have chosen an external coating-based sensing mechanism because of its easy implementation and fabrication process. Gold is used as a plasmonic metal layer with a Nano layer of TiO_2 cemented between the gold layer and PCF. The whole simulation work of our proposed sensor is performed on COMSOL Multiphysics version 6.0, where several simulations are performed to find the best geometrical parameters like air hole size, pitch size, width of gold material, and the thickness of TiO_2. Variations of confinement loss with air hole, plasmonic (gold) layer width, and adhesive TiO_2 layer width are invigilated. This proposed structure has great potential in different fields, such as biomedical and biochemical, to detect low to high RIs.

5.2 Structural design and theoretical model

The cross-section display of proposed sensor structure is mentioned in figure 5.1. We are dealing with dual–core based PCF with different sizes of air holes introduced in the cladding zone. There is a central hole between two cores of radius $r_a = 0.4\ \mu m$. Two holes are presented at both sides of the central hole with radius $r_b = 1.8\ \mu m$, and other holes are presented in the cladding section with a radius $r_c = 1.0\ \mu m$ and $r_d = 1.5\ \mu m$. Four sides of PCF are cut in a C-shape where laminations of the Titanium dioxide (TiO_2) Nano layer and a plasmonic layer of gold (Au) are performed.

In our proposed sensor structure, TiO_2 behaves as an adhesive layer for sensing performance enhancement. The width of the TiO_2 layer and plasmonic layer of Gold (Au) is $t_{Ti_2} = 20\ nm$ and $t_{Au} = 50\ nm$, respectively.

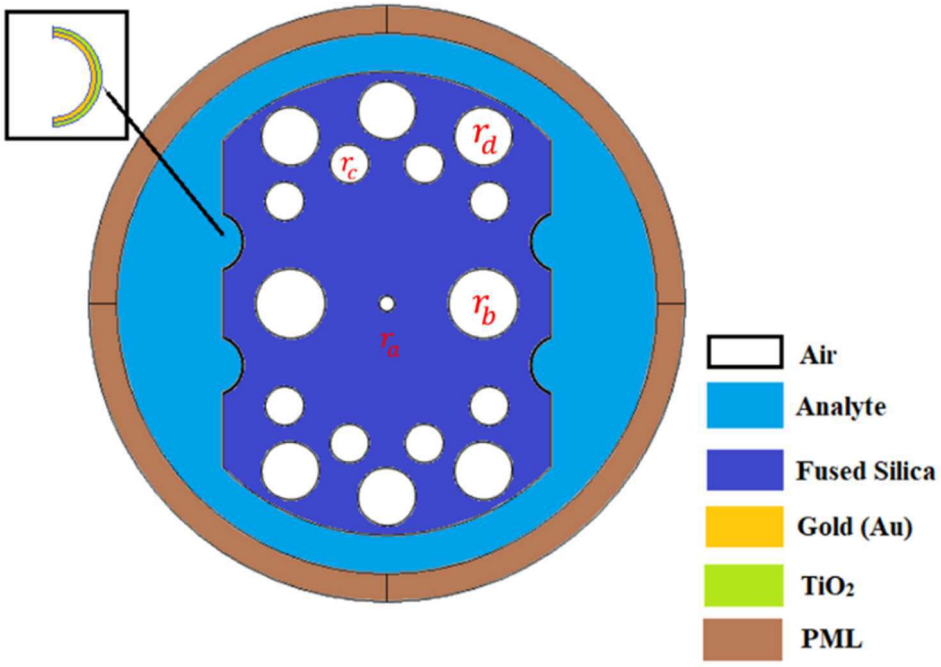

Figure 5.1 A cross-section view of the proposed PCF sensor structure.

Fused silica is one of the best materials for PCF background, so we have chosen it as the background material for our proposed structure, and refractive index of fused silica is specified by following Sellmeier's equation (2.1) [106]. The Drude - Lorentz model has been adopted in our work to compute a frequency-based refractive index (RI) of plasmonic gold material, and its dispersive relation is given by equation (3.1) [173]. Titanium dioxide (TiO_2) has stacked between PCF cladding and plasmonic layer to improve the analyte interaction, (RI) of TiO_2 is calculated from the equation (3.2) [173]. To examine the characteristics of the proposed PCF structure, confinement loss is the crucial factor, and it is given by equation (1.7) [174].

The complete setup of proper working of our PCF sensor using an optical light source, single mode fiber, and the optical spectra analyzer (OSA) is depicted in figure 5.2. Numerical investigation and simulation of our PCF sensor structure are conducted using the finite element method (FEM) and simulation is performed at COMSOL Multiphysics version 6.0 [132]. In this method, the complete cross-section of sensor is disunited into microscopic triangular elements called mesh elements. Using Maxwell's equation, coupled partial differential equations are solved to determine the longitudinal components of the magnetic field and electric fields. To absorb the electromagnetic radiation at the outer surface, the perfect match layer (PML) is applied, and the width of this PML is kept around 10% of the fiber width [105].

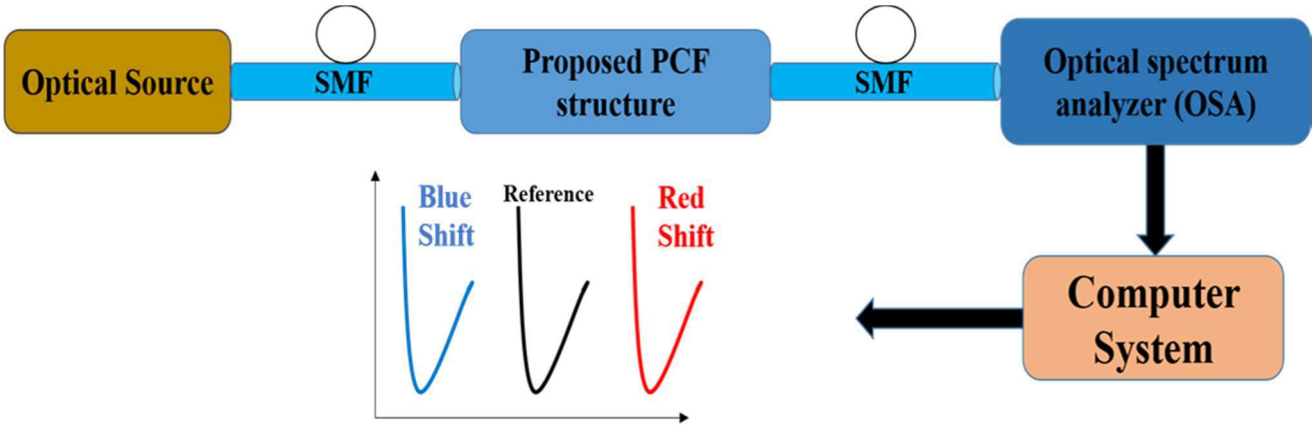

Figure 5.2 The setup of the proposed PCF sensor.

5.3 Result and Discussion

In the simulation process, when (p-polarized) EM – wave starts to pass through the PCF core, the longitudinal part of the electric-field reaches the plasmonic layer and generates an evanescent wave. This wave generates the core – mode along with SPP – mode of PCF, and this dispersion characteristics of both modes are displayed in figure 5.3. It is understandable from figure that moving

towards a red–shift in wavelength coupling strength between core – mode and SPP – mode become more assertive and reach their peak value at a fixed wavelength termed as resonance wavelength. Then it gets the weekend after this peak point. At this resonance wavelength real part of the effective mode index of core mode and the real part of the effective mode index of SPP mode match, and the maximum amount of power is transport from core to SPP mode, named as confinement loss [174].

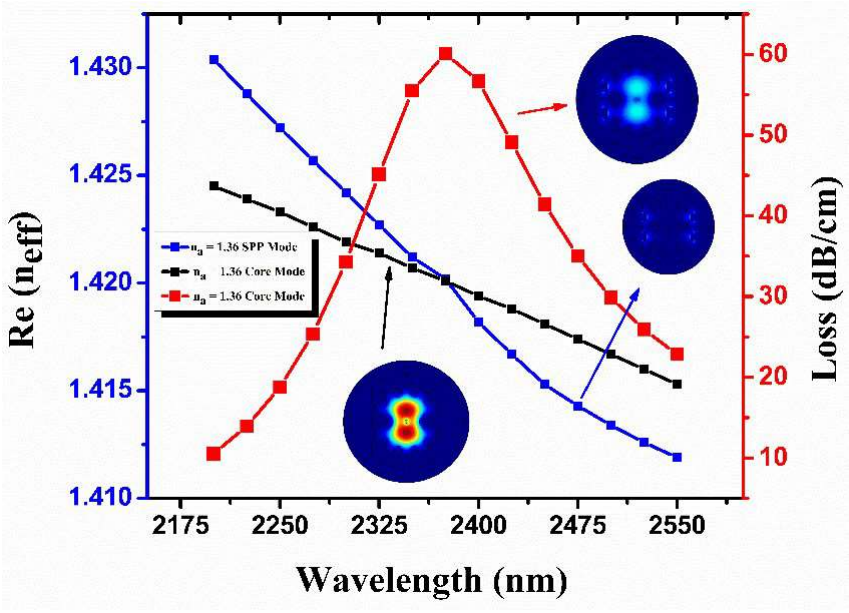

Figure 5.3 Dispersion characteristics plot of core-mode (black color) and SPP-mode (blue color) for the analyte refractive index $n_a = 1.36$, with $r_a = 0.4\ um$, $r_b = 1.8\ um$, $r_c = 1.0\ um$, $r_d = 1.5\ um$, $t_{Au} = 50\ nm$, $t_{TiO_2} = 20\ nm$.

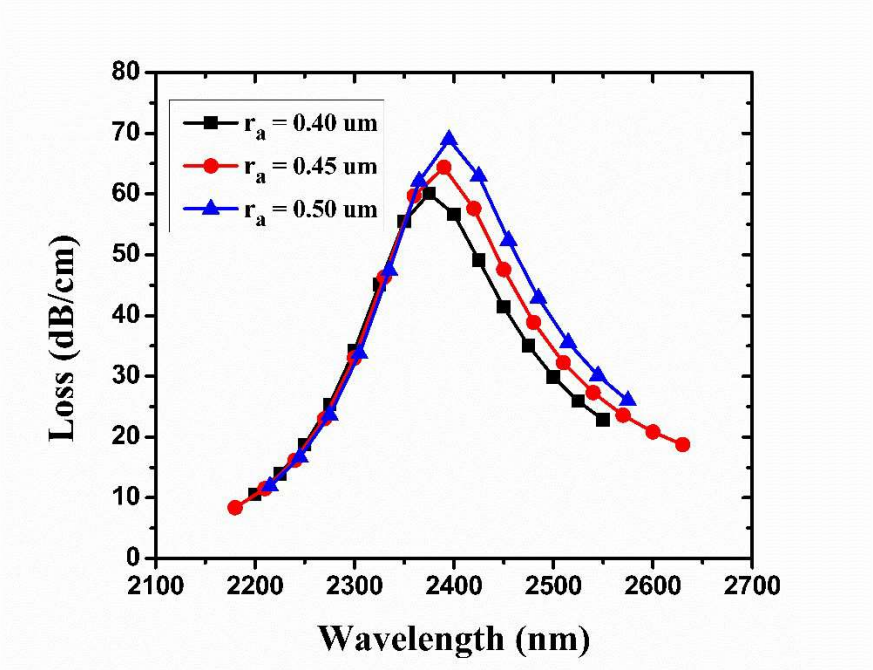

Figure 5.4 Spectra of confinement loss for the central hole radius (r_a) alterations from 0.40 µm to 0.50 µm, with $r_b = 1.8\ um, r_c = 1.0\ um, r_d = 1.5\ um, t_{Au} = 50\ nm, t_{Ti\ 2} = 20\ nm$.

The next task is altering the geometrical parameters of the PCF sensor. We have performed simulations several times to determine the best geometrical parameter for our PCF sensor structure. Figure 5.4 dispose the confinement loss with wavelength for the variations of the radius of the central hole (r_a) from 0.40 µm to 0.50 µm and the confinement loss peaks have a redshift because of escalating air hole size coupling potency between core and SPP modes increases as a consequence of increment in Re (n_{eff}) of SPP-mode [175].

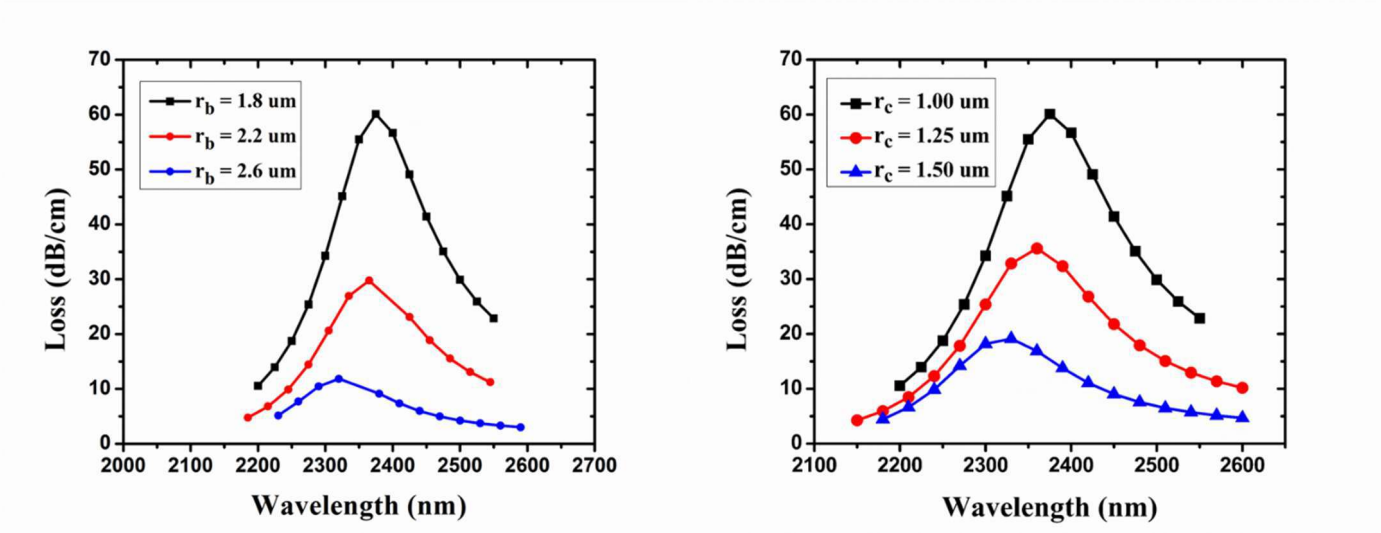

Figure 5.5 Spectra of confinement loss for the variations of air holes radius **(a)** $r_b = 1.8\ um - 2.6\ um$, and **(b)** $r_c = 1.0\ um - 1.5\ um$ with $r_a = 0.4\ um$, $r_d = 1.5\ um$, $t_{Au} = 50\ nm$, $t_{Ti\ _2} = 20\ nm$.

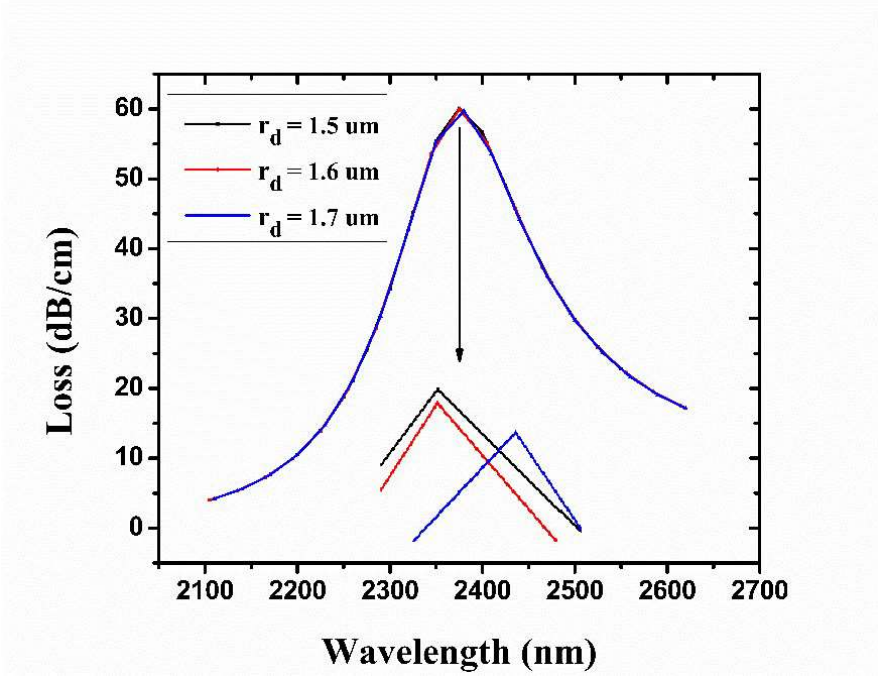

Figure 5.6 Spectra of confinement loss for the variations of air hole radius $r_d = 1.5\ um - 1.7\ um$ with $r_a = 0.4\ um$, $r_b = 1.8\ um$, $r_c = 1.0\ um$, $t_{Au} = 50\ nm$, $t_{Ti\ _2} = 20\ nm$.

Disturbing air hole size in the cladding segment $r_b = 1.8\ um - 2.6\ um$ and $r_c = 1.0\ um - 1.5\ um$, the confinement loss spectrum has a downfall, and depicted in figure 5.5. This happens because raising the size of these air holes makes it difficult for light to reach from the core to SPP modes and weakens the coupling between the two modes mentioned above [176]. Confinement loss spectra remain approximately stable with very low confinement loss variation with the extreme air hole radius (r_d) variations $r_d = 1.50\ \mu m - 1.70\ \mu m$, as shown in figure 5.6. The worthy change is observed with a variation of gold (Au) layer and the sticky layer of TiO_2. Figure 5.7 indicates that the confinement loss reduces from 60.10 dB/cm to 53.56 dB/cm for varying the width of the (Au) metal layer (t_{Au}) from 50 nm - 60 nm with a step size of 5 nm and the analyte RI (n_a) of 1.36. It happens for the reason that on escalating the width of the gold metal layer, high damping loss occurs, resulting in poor penetration of the electric field inside the analyte. Remarkable beneficiation was made by a sticky Nano-layer of TiO_2 [177].

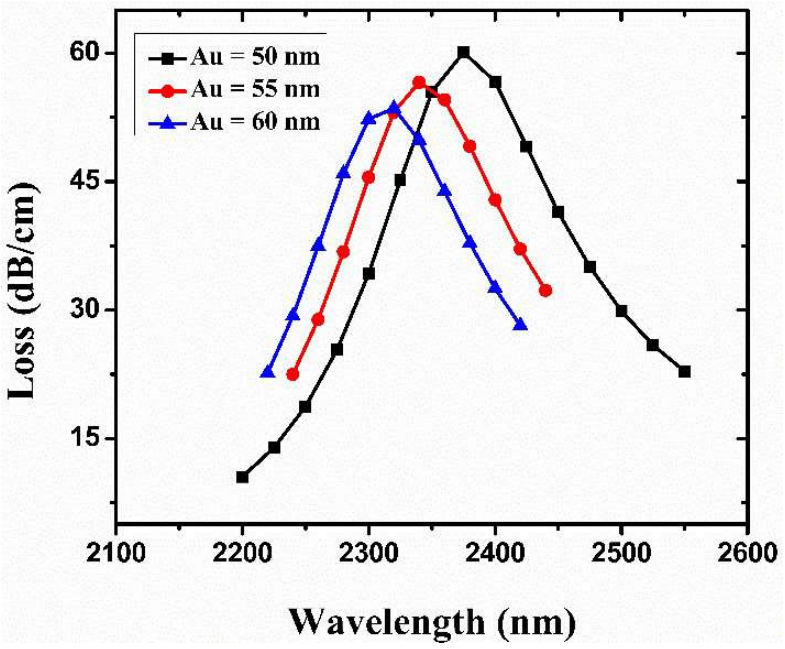

Figure 5.7 Spectra of confinement loss with variable (Au) layer thickness with the analyte RI $n_a = 1.36$ with $r_a = 0.4\ um, r_b = 1.8\ um, r_c = 1.0\ um, r_d = 1.5\ um, t_{TiO_2} = 20\ nm$.

Cementing this TiO_2 Nano layer (working as a catalyst) between PCF and plasmonic layer enhances the coupling strength between core and SPP modes. Hence, the confinement loss peak goes up from 60.10 dB/cm to 80.11 dB/cm with increasing the thickness of TiO_2 from $t_{Ti\ _2} = 20\ nm - 30\ nm$, as mentioned in figure 5.8

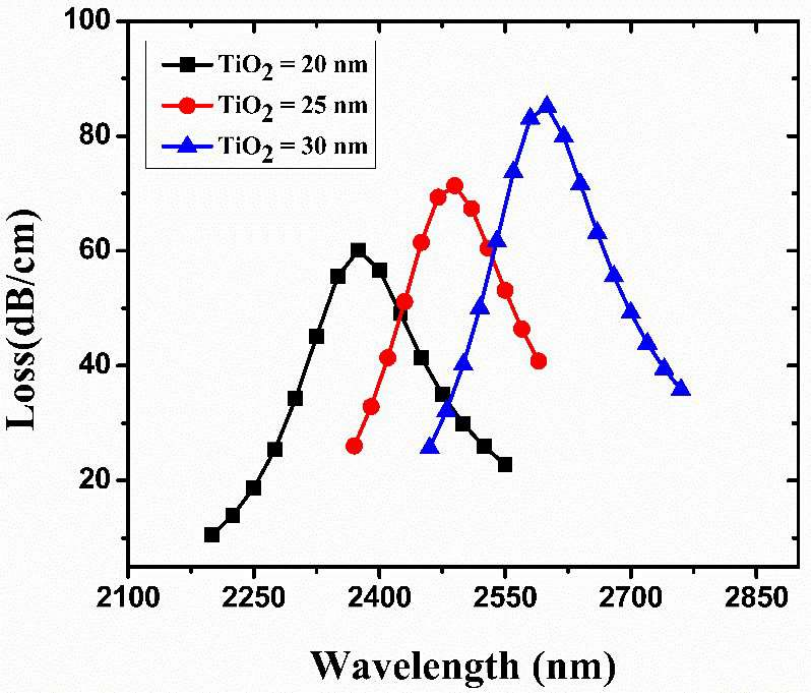

Figure 5.8 Spectra of confinement loss for the variations of TiO_2 layer width with the analyte RI $n_a = 1.36$ with $r_a = 0.4\ um, r_b = 1.8\ um, r_c = 1.0\ um, r_d = 1.5\ um, t_{Au} = 50\ nm$.

The salient key parameter of the PCF sensor is known as wavelength sensitivity (WS), and it is given by equation (2.2) [177]. Our PCF structure is compatible with detecting a wide range of analytes RI $n_a = 1.21 - 1.39$.

We observe that the confinement loss peak value enhances with increasing analyte refractive index because coupling become stronger between core mode and SPP mode with increasing refractive index of analyte [178].

The value of maximum wavelength sensitivity (WS) 35,000 nm/RIU for analyte RI 1.38 – 1.39, and the average wavelength sensitivity 6368 nm/RIU for analyte sample RI $n_a = 1.21 - 1.39$. The distribution of the confinement losses for the variations of the analyte sample RI $n_a = 1.21 - 1.39$ are displayed in figure 5.9.

Another excellent tool to measure the term sensitivity of our sensor is amplitude sensitivity (S_A), which is homogenous to the wavelength sensitivity technique. It is a cost productive method than the wavelength sensitivity (WS) method because spectrum proficiency is not needed like the wavelength sensitivity (WS) method, and all measurement is performed at a defined wavelength. The amplitude sensitivity (S_A) is specified by equation (2.3) [177]**.** The obtained value of amplitude sensitivity for our proposed sensor structure is 373 RIU^{-1} for the analyte sample RI $n_a = 1.38$, as depicted in figure 5.10. A key feature to estimate the performance of the PCF sensor is its resolution, given by the following equation (2.4) [179]**.** Considering the spectrometer resolution $\Delta\lambda_{min} = 0.1\ nm$, we observe the maximum resolution R = 2.85×10^{-6} RIU and the order of detection precision up to 10^{-6} means that the slightest change of order 10^{-6} can be detected for the analyte RI changes.

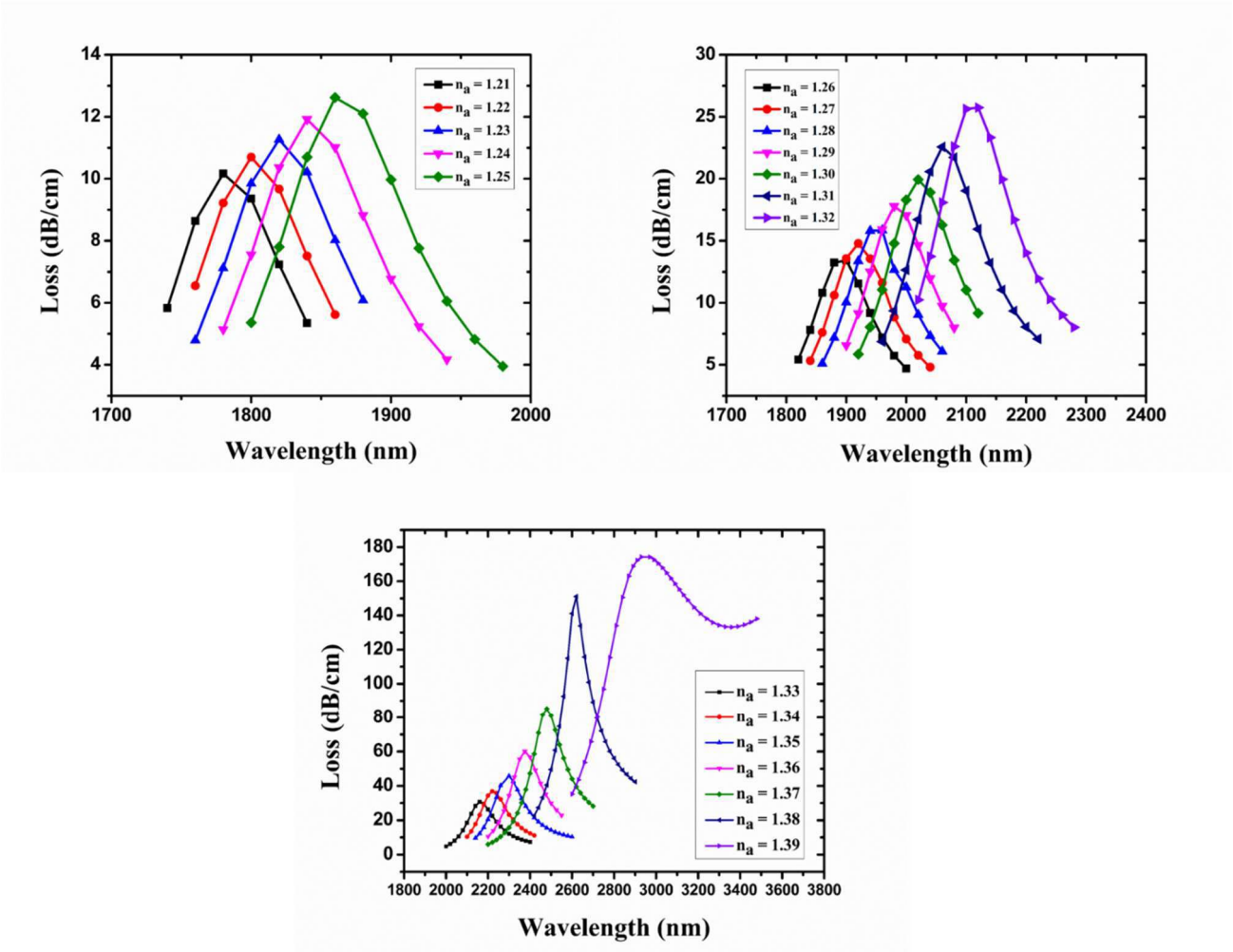

Figure 5.9 Spectra of confinement loss for the variations of the analyte RI n_a = 1.21 to 1.39 with $r_a = 0.4\ um, r_b = 1.8\ um, r_c = 1.0\ um, r_d = 1.5\ um, t_{Au} = 50\ nm, t_{TiO_2} = 20\ nm.$

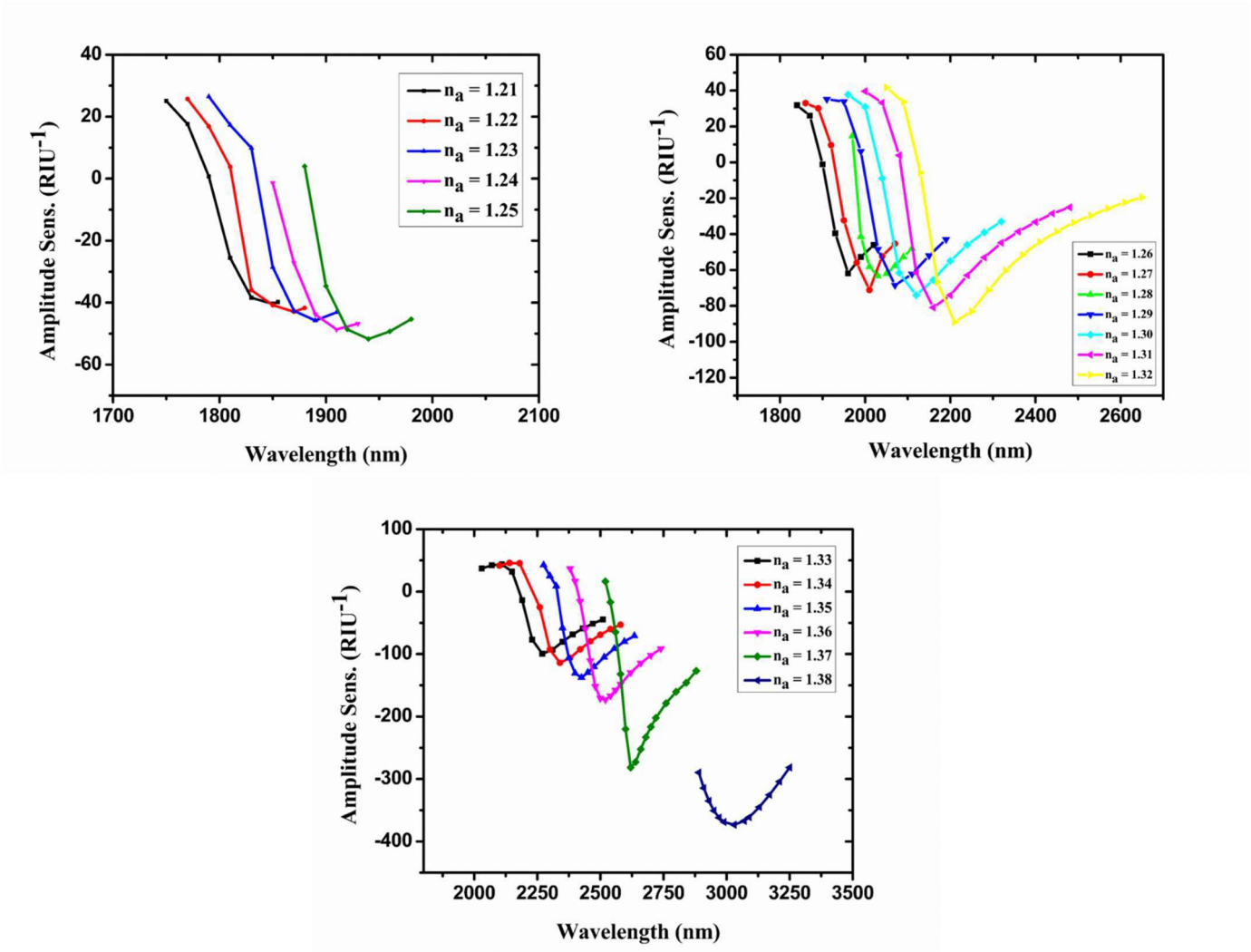

Figure 5.10 The amplitude sensitivity variations for the analyte RI n_a= 1.21 to 1.39 with $r_a = 0.4\ um, r_b = 1.8\ um, r_c = 1.0\ um, r_d = 1.5\ um, t_{Au} = 50\ nm, t_{TiO_2} = 20\ nm$.

A summary of the performance of PCF sensor work for effortless visualization is mentioned in Table 5.1. An extensive contrast of our proposed PCF sensor for the long-range analyte RI with other recently reported PCF RI sensor structures are charted in table 5.2.

Table 5.1 The performance of our PCF sensor for analyte RI range $n_a = 1.21 - 1.39$.

Sample RI	Wavelength (nm)	Res. Peak Shift (nm)	Wave. Sens. (nm/RIU)	Amp. Sens. (RIU^{-1})	Sensor Resolution	Figure of Merit (RIU^{-1})
1.21	1780	20	2000	-40	5.00×10^{-5}	43
1.22	1800	20	2000	-43	5.00×10^{-5}	42
1.23	1820	20	2000	-46	5.00×10^{-5}	27
1.24	1840	20	2000	-49	5.00×10^{-5}	27
1.25	1860	40	4000	-52	2.50×10^{-5}	48
1.26	1900	20	2000	-62	5.00×10^{-5}	22
1.27	1920	40	4000	-71	2.50×10^{-5}	41
1.28	1960	20	2000	-63	5.00×10^{-5}	19
1.29	1980	40	4000	-69	2.50×10^{-5}	40
1.30	2020	40	4000	-74	2.50×10^{-5}	34
1.31	2060	60	6000	-81	1.67×10^{-5}	50
1.32	2120	40	4000	-89	2.50×10^{-5}	36
1.33	2160	60	6000	-100	1.67×10^{-5}	41
1.34	2220	80	8000	-114	1.25×10^{-5}	59
1.35	2300	75	7500	-138	1.33×10^{-5}	47
1.36	2375	105	10500	-173	9.52×10^{-6}	65
1.37	2480	140	14000	-281	7.14×10^{-6}	78
1.38	2620	350	35000	-373	2.85×10^{-6}	259
1.39	2970	----	----	----	----	----

Full-width half maxima (FWHM) is a crucial parameter used to compute the figure of merit (FOM) of our PCF sensor structure. A high value of FOM for a proposed PCF sensor structure indicates high performance and possible practical realization. The following equation (3.3) gives the term FOM [112]. We have analyzed the sensitivity and FWHM for a particular analyte RI. For analyte RI 1.38, the sensitivity value is 35,000 nm/RIU, and FWHM is 135.31 nm, putting these values in eq. (5.8) we get the FOM value of around 259 (RIU^{-1}) for our PCF sensor structure, as depicted in figure 5.11.

Table 5.2 The performance comparison of our PCF sensor with recently reported PCF sensor solely based on simulation

Reference	Model Structure	Analyte RI range	Wave. Sens. (nm/RIU)	Amp. Sens. (RIU^{-1})	Wave. Resolution (RIU)	Publication year
[180]	D - shape PCF sensor	1.33 -1.39	11500	230	8.7×10^{-6}	2020
[181]	Broad-range PCF sensor	1.35-1.40	10000	1115	2.00×10^{-5}	2022
[179]	D – shape PCF sensor	1.30-1.38	4250	NA	2.35×10^{-5}	2022
[182]	Open channel PCF sensor	1.33-1.40	7000	594	1.43×10^{-5}	2023
[183]	Arc – shape PCF sensor	1.32-1.37	14100	109	9.17×10^{-6}	2023
[184]	High perf. PCF sensor	1.29-1.34	13800	2380	7.24×10^{-6}	2023
This Work	Dual Core PCF sensor	1.21-1.39	35000	373	2.85×10^{-6}	

Since our proposed PCF sensor structure has an extensive analyte RI range $n_a = 1.21 - 1.39$ detection, which may be applied in different fields such as biomedical and biochemical, and other different kinds of chemicals. Our sensor can be implemented to see the different types of organics which contains fluorine and have a low refractive index value ($n_a < 1.30$) such as 2, 2, 2, trifluoroethyl trifluoroacetate ($n_a = 1.2812$), trifluoroacetic acid ($n_a = 1.2850$), 1, 1, 1, 3, 3, 3 – hexafluoro-2-propanol ($n_a = 1.275$) [179].

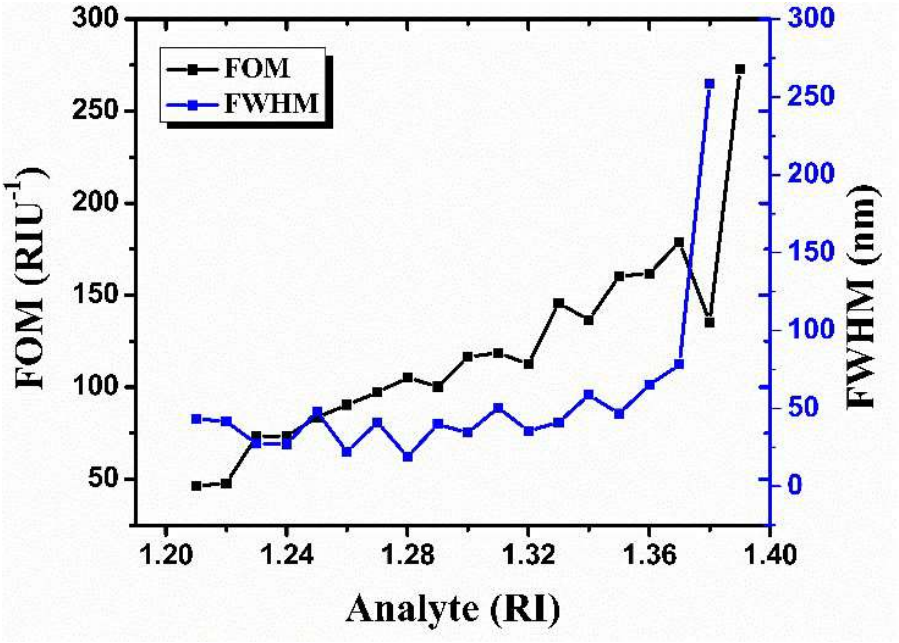

Figure 5.11 The distributions of FOM and FWHM for analyte RI (n_a) variations from 1.21 to 1.39, with $r_a = 0.4\ um$, $r_b = 1.8\ um$, $r_c = 1.0\ um$, $r_d = 1.5\ um$, $t_{Au} = 50\ nm$, $t_{Ti\ \ 2} = 20\ nm$.

Nowadays, a significant issue in the medical field is detecting the cancer cell early for appropriate treatment. Several cancer cell tissues, such as cervical cancer, blood cancer, breast cancer, adrenal–gland cancer, skin cancer, etc., are reported for different types of cancer cells [185]. Their refractive index lies in the range 1.36 – 1.39, and our proposed sensor structure is designed for this analyte range detection. A pregnancy test based on the refractive index can also be performed using our proposed PCF structure. The refractive index of urine can be tested by putting a few drops of urine sample in the sensing area of our sensor. The general urine examination (GUE) test results show that all other factors remain the same such as glucose level, protein level, uric acid, etc. The detection of RI of the urine sample is most beneficial because the urine RI increases during pregnancy, and this increment is due to pregnancy Harmon [186]. The next application of the proposed sensor structure in the row is alcohol detection by varying its concentration in water.

The refractive index of water with 0% of alcohol is 1.333. The refractive index of water mixed with alcohol varies from 1.3384, 1.3450, 1.3550, and so on for changing the concentration of alcohol in water, such as 10%, 20%, 30%, and so on, respectively [187]. So this range can easily be identified with the help of the proposed PCF sensor because of its compatibility with this detection range.

Figure 5.12 represents the variations of the resonance wavelength with the analyte RI $n_a = 1.21 - 1.39$, and its 3rd – order polynomial fitting. Correlation between the analyte RI and resonance wavelength (λ_{res}) for polynomial fitting is given by the equation $y = intercept + (B1 \times x^1) + (B2 \times x^2) + (B3 \times x^3)$. In this equation, the y-axis represents the resonance wavelength (λ_{res}), and the x-axis represents the analyte RI. The values of intercept represented by B_1, B_2, and B_3 are mentioned in figure 5.12. It is clear from the figure the statistical value of R^2 is 0.98293, which indicates the better fitting arrangement for our PCF sensor.

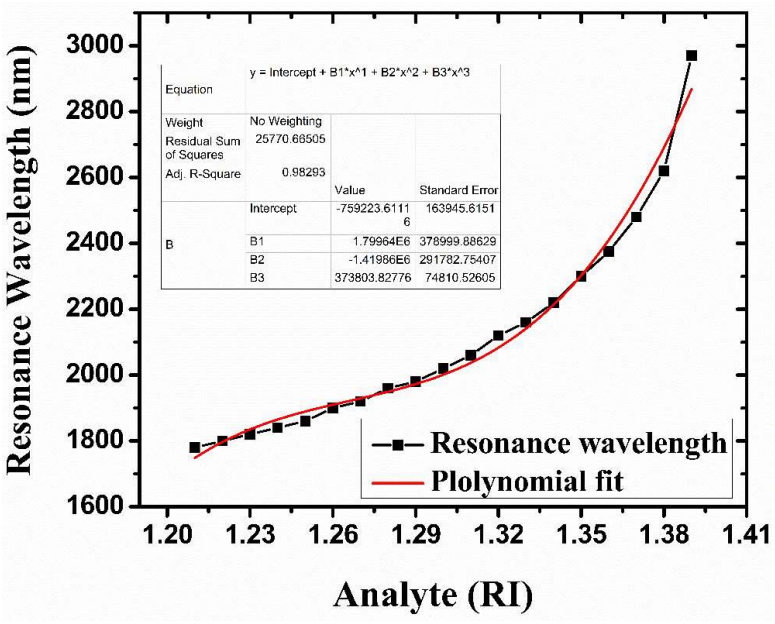

Figure 5.12 The variation of resonance wavelength and polynomial fit with the change in the analyte RI.

5.4 Fabrication method

PCF can be fabricated by several well-defined available technologies where a macroscopic preform of the desired shape is modulated and then drawn on microscopic scale fiber. The available technologies for this task are extrusion [188], injection molding [189], sol–gel method [190], and stack and draw process [100]. Among these available technologies, the stack-and-draw method for PCF fabrication is the most promising, fast, clean, and cost-effective technology. This process has a few steps; the first step is fabrication, where capillaries of desired diameters are fabricated. Then in the second step, they are stacked according to the required Core cladding structure. After this process, the preform is extracted as microstructure rods and finally to a fiber in the last step. This process continues to repeat until we get desired structure shape and parameters (diameter of fiber, air hole size, pitch) of the proposed PCF sensor. The subsequent work in sensor fabrication is to coat a plasmonic layer of gold and an adhesive layer of TiO_2. There are some approved technologies for the deposition of Nano layers, such as wet–chemistry deposition, thermal evaporation, and radio frequency sputtering [191]. However, these methods undergo intense surface roughness due to a lack of uniformity of the Nano layer. That is why the chemical vapor deposition (CVD) method is better than the above mentioned technologies [137].

5.5 Conclusion

We have put forward the surface plasmon resonance phenomenon based Dual-core PCF sensor for detecting wide-range analyte RI of 1.21 to 1.39. The beauty of our simulation work of the proposed design is to reveal the sensing performance for long-range analyte RI. It provides a maximum wavelength sensitivity of 35000 nm/RIU for analyte RI 1.38 to 1.39, and maximum amplitude sensitivity of 373 RIU^{-1}. The wavelength resolution is the order of 10^{-6} for analyte RI.

The figure of merit is observed with the maximum value of 259 RIU^{-1}, which reveals the degree of performance of the proposed sensor. Regression analysis from polynomial curve fitting provides the maximum value of R^2 of 0.98293. Fabrication has become more accessible and fast due to the availability of recently developed technologies like the stack and draws method. From an application point of view, the proposed PCF sensor has the potential to work in different fields, such as biomedical and biochemical, for the detection of low refractive index range chemicals. The proposed PCF sensor may be utilized to reveal the stimulating application for pregnancy and alcohol tests.